Journal of Magnetism and Magnetic Materials 497 (2020) 166015

Contents lists available at ScienceDirect

Journal of Magnetism and Magnetic Materials

journal homepage: www.elsevier.com/locate/jmmm

Research articles

Magnetocaloric difference between ribbon and bulk shape of Gd-based metallic glasses

Lin Xue[a], Qiang Luo[a], Liliang Shao[a], Baolong Shen[a,b,*]

[a] School of Materials Science and Engineering, Jiangsu Key Laboratory for Advanced Metallic Materials, Southeast University, Nanjing 211189, China
[b] Institute of Massive Amorphous Metal Science, China University of Mining and Technology, Xuzhou 221116, China

ARTICLE INFO

Keywords:
Amorphous alloys
Magnetocaloric effect
Demagnetizing field
Oxides

ABSTRACT

In this work, magnetocaloric properties of the as-cast rods and melt-spun ribbons for Gd-based metallic glasses are investigated. Different magnetocaloric responses in the rods and ribbons are observed and discussed. Under a magnetic field change of 5 T, maximum magnetic entropy change ($-\Delta S_M^{max}$) values of 8.7 and 9.1 $Jkg^{-1}K^{-1}$ are obtained for the as-cast $Gd_{55}Co_{19}Al_{24}Si_1Fe_1$ and $Gd_{20}Dy_{20}Er_{20}Co_{20}Al_{20}$ rods, which are obviously larger than those of 7.8 and 7.7 $Jkg^{-1}K^{-1}$ for their ribbon counterparts, respectively. In addition, the as-cast rods show obviously larger exponent n values compared with the melt-spun ribbons, i.e., the $-\Delta S_M^{max}$ increases faster with increasing applied magnetic field. The magnetocaloric difference is analyzed and can be mainly attributed to the effects of the demagnetizing field, the oxide existence and the microstructural differences in ribbons and rods. The glassy rods exhibiting larger magnetocaloric effect are more attractive for the application of magnetic refrigerants.

1. Introduction

Magnetocaloric effect (MCE) is detected as the heating or cooling of magnetic materials derived from the magnetic ordering or disordering under a varying magnetic field. Magnetic refrigeration based on MCE exhibits relatively high refrigeration efficiency and eco-friendliness, which makes magnetic refrigeration one of the most extensive research subjects both in condensed matter physics and material science [1–6]. Compared with $Gd_5(Si, Ge)_4$ compounds, $La(Fe, Si)_{13}$ type alloys and NiMn-based Heusler alloys [7–9] exhibiting giant MCE in a narrow temperature range around the Curie temperature (T_C) but large hysteresis and loss, materials with second order phase transition, like pure Gd and amorphous alloys exhibiting a broader transition temperature range accompanied with negligible thermal and magnetic hysteresis, are conducive to magnetic refrigerators designed with Ericsson cycle [1,2]. Due to the unique properties superior to the crystalline alloys, such as tunable T_C with modulatory compositions, high corrosion resistance, as well as fine molding and processing behavior, metallic glasses (MGs) have attracted intense interest in magnetocaloric material researches [2,10]. In the past decades, effect of constituents, structure, effective magnetic moment and applied magnetic field on the MCE of MGs have been widely studied. Especially, a number of rare earth (RE, e.g. Gd, Tb, Dy, Ho and Er)-based glassy alloys showing large MCE have been developed, and field dependence of MCE as well as universal curves were well established for predictions of refrigerant systems [11–13].

Since the first amorphous alloy was prepared by Duwez using quenching method, fast cooling techniques have been generally used to produce amorphous alloys, including melt spinning, cooper mold casting and melt-extraction methods, etc. [14–16]. Samples prepared in bulk, ribbon, particle and wire-shaped forms showing different MCE responses were investigated [16–19]. Amorphous samples with the same composition obtained by these different preparing methods can show differences in microstructures that affect MCE [15,17,20]. In addition, several factors during the preparation can also influence the MCE of the alloys, such as the sample geometry and the remnant impurities or contamination [18,20,21]. It was reported that there is always a layer of native oxides on top of the glass surface or even oxide impurities in the inner part, especially MGs containing reactive RE metals [6,22–24]. In this work, the differences in magnetocaloric behaviors between the as-cast rods and melt-spun ribbons of $Gd_{55}Co_{19}Al_{24}Si_1Fe_1$ [25] and $Gd_{20}Dy_{20}Er_{20}Co_{20}Al_{20}$ [26] MGs were studied, and the influence of demagnetizing field and oxygen effect on the magnetic behavior was investigated.

* Corresponding author at: School of Materials Science and Engineering, Jiangsu Key Laboratory for Advanced Metallic Materials, Southeast University, Nanjing 211189, China.
E-mail address: blshen@seu.edu.cn (B. Shen).

https://doi.org/10.1016/j.jmmm.2019.166015
Received 23 July 2019; Received in revised form 30 September 2019; Accepted 19 October 2019
Available online 22 October 2019

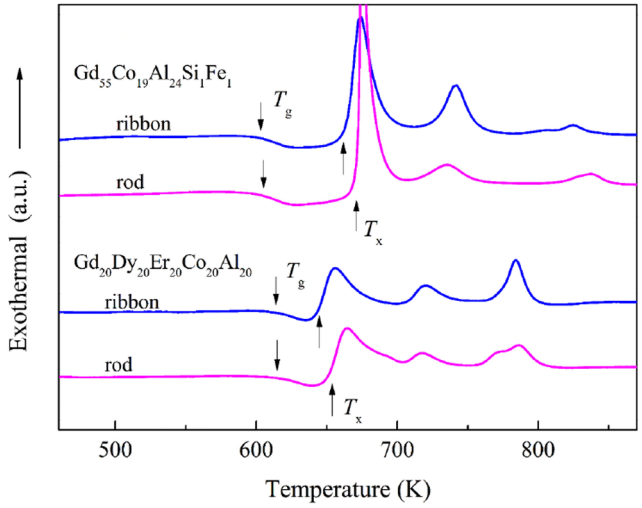

Fig. 1. DSC traces of the as-cast rods and melt-spun ribbons for $Gd_{55}Co_{20}Al_{24}Si_1Fe_1$ and $Gd_{20}Dy_{20}Er_{20}Co_{20}Al_{20}$ alloys.

2. Experimental

Mother alloy ingots with nominal compositions of $Gd_{55}Co_{19}Al_{24}Si_1Fe_1$ and $Gd_{20}Dy_{20}Er_{20}Co_{20}Al_{20}$ were prepared by arc-melting a mixture of raw materials with purities above 99.9 wt% under high purity argon atmosphere. Ribbons with a width of 1.5 mm and a thickness of 35 μm were produced by single-roller melt spinning method, and cylindrical rods with a diameter of 1 mm were prepared by copper mold casting method. Both the ribbons and rods were prepared under vacuum condition about 8×10^{-3} Pa. Amorphous nature of both the as-cast rods and melt-spun ribbons was confirmed within the sensitivity limitation of X-ray diffraction (XRD, Bruker D8 Advancer) with Cu Kα radiation. Thermal analyses were performed by differential scanning calorimetry (DSC, NETZSCH 404 F3) and magnetic properties were measured using a Magnetic Properties Measurement System (MPMS, Quantum Design). In addition, the ribbons were aligned with the applied field contained in its plane, and magnetic field was applied along the axial direction of rods. The morphology and elemental composition of surface and inner part for the ribbons and rods were detected using a scanning electron microscope (SEM, FEI Sirion 200) using an energy dispersive spectrometer (EDS). The ribbon and rod samples for inner part detection were polished before measurement, and the thickness of the polished ribbon is about 20 μm. The oxygen content of the melt-spun ribbons and as-cast rods was analyzed using an O/N Analyzer (Leco CS844).

3. Results and discussion

Fig. 1 displays the DSC traces of melt-spun ribbons and as-cast rods for $Gd_{55}Co_{19}Al_{24}Si_1Fe_1$ and $Gd_{20}Dy_{20}Er_{20}Co_{20}Al_{20}$ alloys. Glass transition followed by several crystallization exothermic peaks can be observed in all the detected samples. No obvious difference in glass transition temperature (T_g) is observed between ribbons and rods while the ribbons show lower initial crystallization temperatures (T_x) than those of their rod counterparts, as listed in Table 1, and thus larger supercooled liquid regions ($\Delta T_x = T_x - T_g$) are obtained in the as-cast rods. The crystallization enthalpies of the samples are calculated, and a slight larger crystallization enthalpy can be found in the rods as listed in Table 1 as well. No detectable sharp Bragg peaks corresponding to crystalline phases in both the ribbons and rods are detected, therefore differences in microstructures that influence the crystallization should be conjectured in the prepared ribbons and rods.

Temperature dependence of magnetization (*M-T*) curves for both the ribbons and rods under an applied magnetic field of 0.02 T for $Gd_{55}Co_{19}Al_{24}Si_1Fe_1$ and $Gd_{20}Dy_{20}Er_{20}Co_{20}Al_{20}$ alloys are shown in Fig. 2(a) and (b), respectively. An obvious ferromagnetic to paramagnetic phase transition over the measured temperature regime can be seen in each sample. Determined from the minimum of dM/dT curves, the as-cast rod and melt-spun ribbon exhibit almost the same T_C as listed in Table 1. As shown in Fig. 2(a) and (b), the magnetization curves of the ribbon and rod samples overlap above the T_C whereas divaricate obviously below T_C, and the rods show obviously lower magnetizations than those of the ribbon counterparts. This could be attributed to the effect of demagnetizing field in the rods with large diameter to length ratio [21] and other possible magnetic anisotropy. The reciprocal susceptibility for the samples is illustrated in the upper right insets in Fig. 2(a) and (b). Linear relationship between the reciprocal susceptibility and the temperature at high temperature region can be seen for each sample, which obeys a typical Curie-Weiss law. The Curie-Weiss fitting results of positive Weiss constants (θ_P) verify the ferromagnetic-paramagnetic phase transition in the samples. Despite the smaller magnetization, larger effective moment (μ_{eff}) values are obtained for the rods (7.4 and 8.8 μ_B for $Gd_{55}Co_{19}Al_{24}Si_1Fe_1$ and $Gd_{20}Dy_{20}Er_{20}Co_{20}Al_{20}$, respectively) compared with their ribbon counterparts (6.5 and 7.3 μ_B for $Gd_{55}Co_{19}Al_{24}Si_1Fe_1$ and $Gd_{20}Dy_{20}Er_{20}Co_{20}Al_{20}$, respectively). Generally, a larger μ_{eff} value often corresponds to a more distinct magnetocaloric response in a magnetic refrigerant, therefore larger magnetic entropy change (ΔS_M) values can be expected in the as-cast rods under a certain magnetic field. Additionally, it is worth noting that the magnetization of the rod of $Gd_{55}Co_{19}Al_{24}Si_1Fe_1$ keeps constant below T_C as shown in Fig. 2(a), which is also observed in other works [27–29]. *M-T* curves of $Gd_{55}Co_{19}Al_{24}Si_1Fe_1$ rod under different applied fields were measured and shown in the lower left inset in Fig. 2(a). It can be seen that the magnetization increases and the curve tends to be smooth like that of the ribbon as the applied magnetic field increases.

Hysteresis loops under a magnetic field of 5 T at 5 and 300 K were measured for the rod and ribbon of $Gd_{55}Co_{19}Al_{24}Si_1Fe_1$ alloy as shown in Fig. 3. Both the melt-spun ribbon and as-cast rod exhibit ferromagnetic performance at low temperature while paramagnetic character at

Table 1
The glass transition temperature (T_g), crystallization temperature (T_x), supercooled liquid region ($\Delta T_x = T_x - T_g$), crystallization enthalpy (ΔH), Curie temperature (T_C), maximum magnetic entropy change ($-\Delta S_M^{max}$), refrigeration capacity (RC) under a magnetic field change of 5 T, and exponent n of as-cast rods and melt-spun ribbons of $Gd_{55}Co_{19}Al_{24}Si_1Fe_1$ and $Gd_{20}Dy_{20}Er_{20}Co_{20}Al_{20}$ alloys compared with some other Gd-based alloys.

Sample	T_g (K)	T_x (K)	ΔT_x (K)	ΔH (J/g)	T_C (K)	$-\Delta S_M^{max}$ (J kg^{-1}K^{-1})	RC (J kg^{-1})	n	Oxygen content (%)	Refs.
$Gd_{55}Co_{19}Al_{24}Si_1Fe_1$-ribbon	600	664	64	49.7	107	7.8	749	0.73	0.1693	This work
$Gd_{55}Co_{19}Al_{24}Si_1Fe_1$-rod	598	672	74	50.8	108	8.7	810	0.77	0.1527	This work
$Gd_{20}Dy_{20}Er_{20}Co_{20}Al_{20}$-ribbon	610	642	32	48.9	42	7.7	523	0.84	0.4836	This work
$Gd_{20}Dy_{20}Er_{20}Co_{20}Al_{20}$-rod	611	649	37	51.6	43	9.1	619	0.90	0.2987	This work
$Gd_{55}Ni_{20}Al_{25}$	588	642	54	–	71	7.98	782	–	–	[12]
$Gd_{20}Ho_{20}Er_{20}Co_{20}Al_{20}$	612	652	40	–	37	11.2	627	0.85	–	[13]
$Gd_{52.5}Co_{16.5}Al_{31}$	601	671	70	–	95	9.8	910	–	–	[19]
$Gd_{55}Ni_{25}Al_{18}Zn_2$	552	591	39	–	82.5	9.33	849	0.90	–	[28]

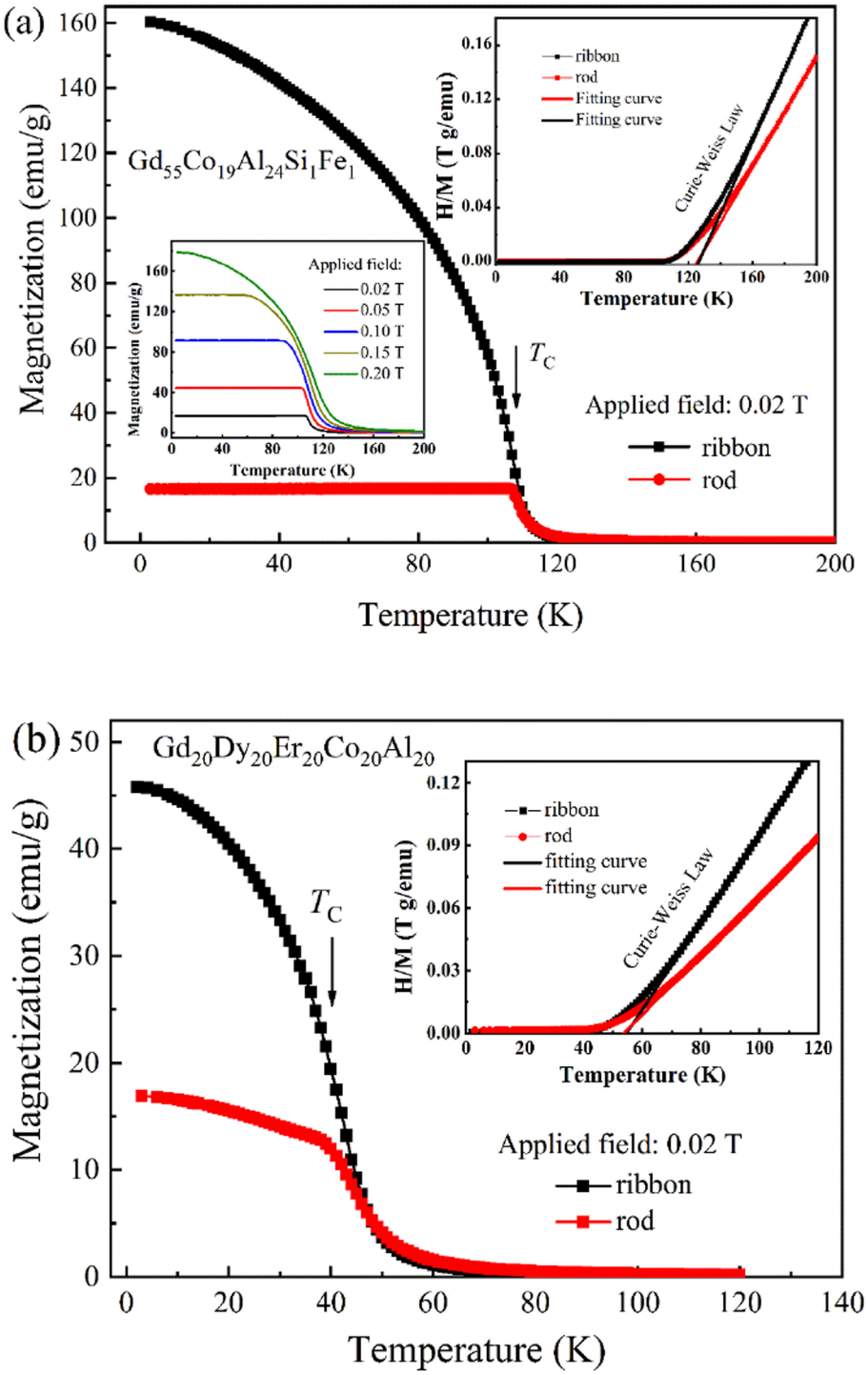

Fig. 2. Temperature dependence of magnetization curves for $Gd_{55}Co_{20}Al_{24}Si_1Fe_1$ (a) and $Gd_{20}Dy_{20}Er_{20}Co_{20}Al_{20}$ alloys (b) under a field of 0.02 T. The left bottom inset in (a) shows the temperature dependence of magnetization curves for $Gd_{55}Co_{20}Al_{24}Si_1Fe_1$ alloy under different applied field. The upper right insets show the plots of *H/M* ratio versus temperature.

room temperature. In addition, distinct soft magnetic characteristics, for instance, large saturation magnetization, overlapping loops and negligible coercivity (about 0.0035 T as shown in the inset) can be seen, demonstrating a negligible hysteresis loss that is favorable to refrigerant applications. As the applied field increases, both the ribbon and rod are magnetized and get saturated rapidly under a low magnetic field. Owing to the influence of demagnetizing field, the rod sample get saturated at higher applied field compared with the ribbon counterpart [28]. Nevertheless, the as-cast rod shows obviously higher saturation magnetization than that of the ribbon.

Isothermal magnetization (*M-H*) curves for $Gd_{55}Co_{19}Al_{24}Si_1Fe_1$ and $Gd_{20}Dy_{20}Er_{20}Co_{20}Al_{20}$ alloys were measured under a varying magnetic field of 0–5 T at a series of temperatures. The sweep rate was slow enough to ensure that the data were obtained in an isothermal condition. As displayed in Fig. 4, a ferromagnetic-paramagnetic phase transition is verified in all the ribbons and rods, which is in accordance with their *M-T* curves. Furthermore, smaller susceptibilities but higher saturation magnetizations in the rods can be seen by contrast with their

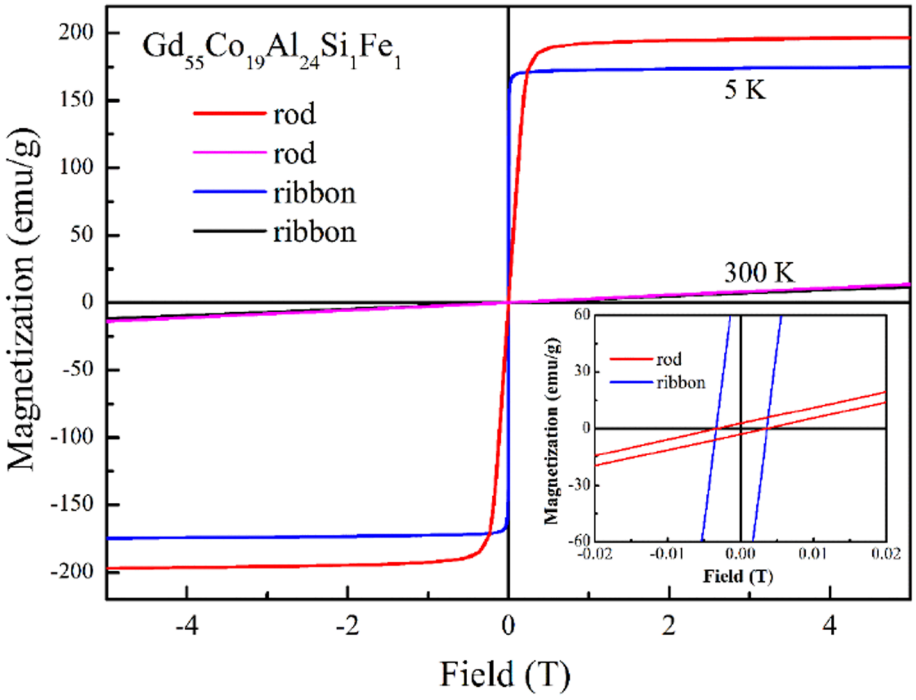

Fig. 3. The hysteresis loop of the as-cast rod and melt-spun ribbon for $Gd_{55}Co_{20}Al_{24}Si_1Fe_1$ alloy at 5 and 300 K, respectively. The inset exhibits the amplification around zero field.

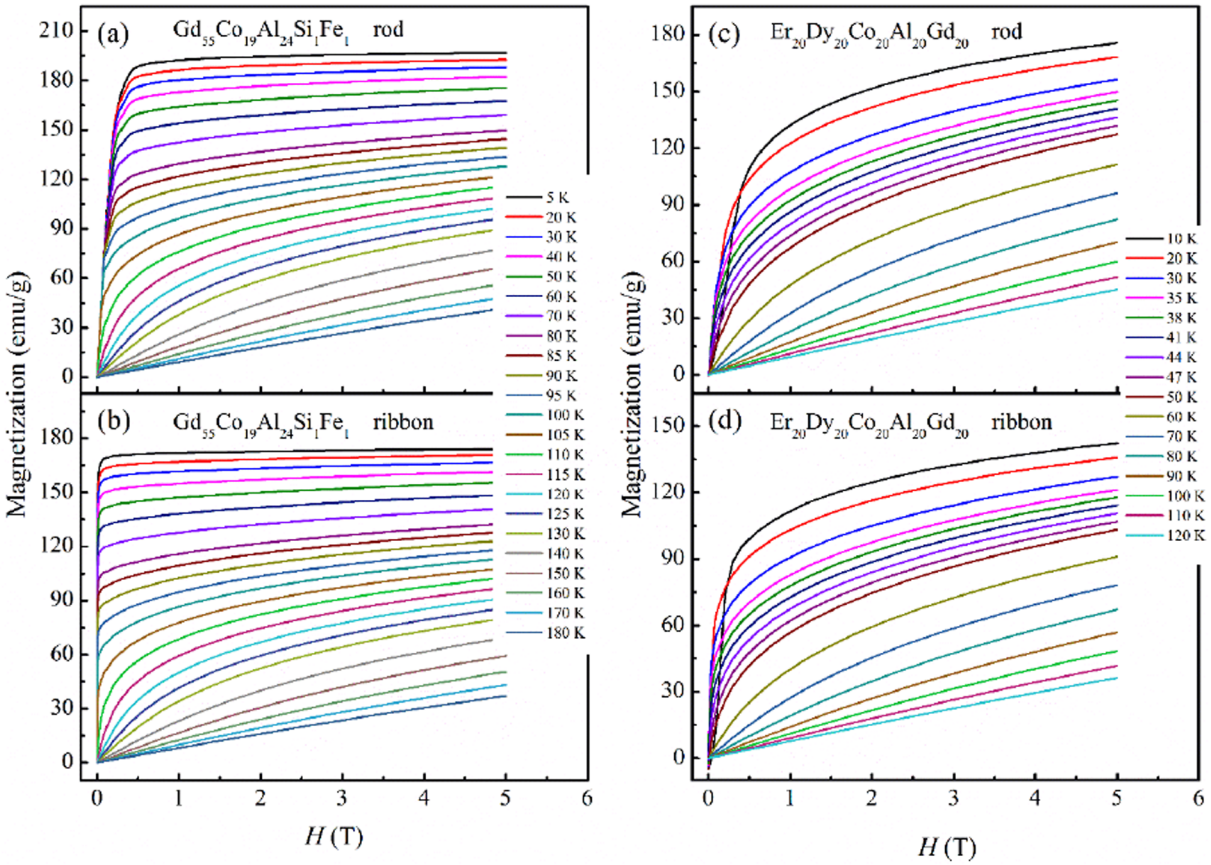

Fig. 4. Isothermal magnetization curves for the as-cast rods and melt-spun ribbons of $Gd_{55}Co_{20}Al_{24}Si_1Fe_1$ and $Gd_{20}Dy_{20}Er_{20}Co_{20}Al_{20}$ alloys.

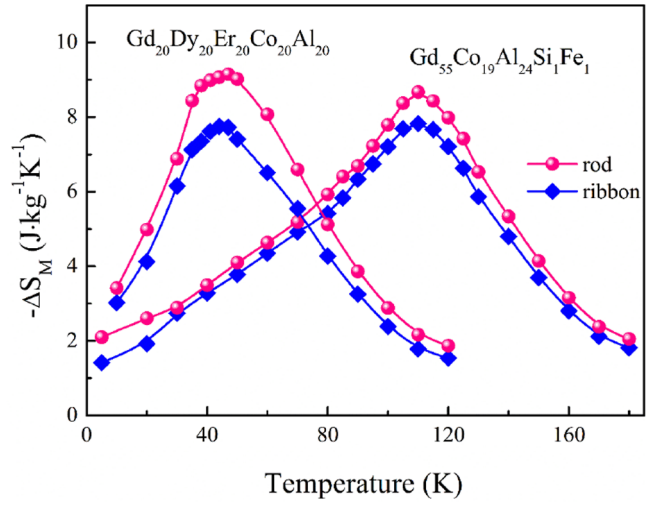

Fig. 5. Magnetic entropy changes versus temperature for the as-cast rods and melt-spun ribbons of $Gd_{55}Co_{20}Al_{24}Si_1Fe_1$ and $Gd_{20}Dy_{20}Er_{20}Co_{20}Al_{20}$ alloys under a field change of 5 T.

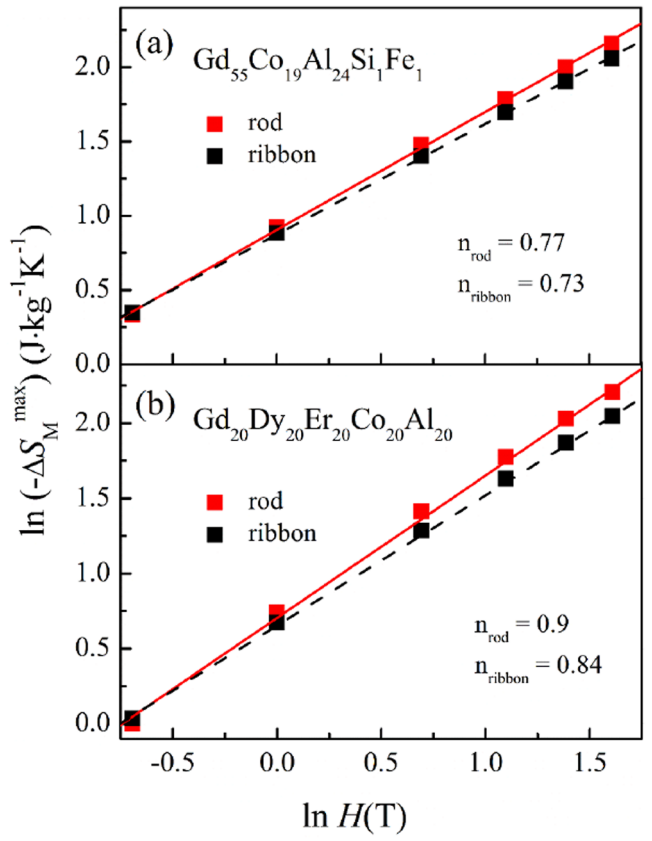

Fig. 6. The maximum magnetic entropy change as a function of the applied field for the as-cast rods and melt-spun ribbons of $Gd_{55}Co_{20}Al_{24}Si_1Fe_1$ (a) and $Gd_{20}Dy_{20}Er_{20}Co_{20}Al_{20}$ (b) alloys.

ribbon counterparts. The MCE of a refrigerant is mainly evaluated by the ΔS_M, which can be derived from Maxwell relation by integrating over the isothermal *M-H* curves [1]:

$$\Delta S_M(T, \mu_0 H) = S(T, \mu_0 H) - S(T, 0) = \mu_0 \int_{H_{min}}^{H_{max}} \frac{\partial M}{\partial T} dH \quad (1)$$

where H_{max} and H_{min} represent the maximum and minimum values of the applied magnetic field, and H_{min} is defined as 0 T in this work. According to Eq. (1), $-\Delta S_M$ as a function of temperature with magnetic field change of 5 T were calculated for $Gd_{55}Co_{19}Al_{24}Si_1Fe_1$ and $Gd_{20}Dy_{20}Er_{20}Co_{20}Al_{20}$ alloys, respectively, as shown in Fig. 5. It can be seen that the $-\Delta S_M^{max}$ locates in the vicinity of T_C for all the samples. It is obviously that the rods exhibit larger $-\Delta S_M$ values than the ribbons. In particular, larger difference values between ribbons and rods is obtained in the $Gd_{20}Dy_{20}Er_{20}Co_{20}Al_{20}$ alloy. Additionally, refrigeration capacity (*RC*) is another important parameter usually used to estimate the MCE [1],

$$RCP = -\Delta S_M^{max} \times \delta T_{FWHM} \quad (2)$$

where δT_{FWHM} is the full width at half $-\Delta S_M^{max}$. The calculated $-\Delta S_M^{max}$ and *RC* values under magnetic field of 5 T for both ribbons and rods are listed in Table 1. Obviously, larger $-\Delta S_M^{max}$ and *RC* values are obtained in the as-cast rods rather than the melt-spun ribbons.

For materials with second order phase transition, the $-\Delta S_M^{max}$ value increases with increasing applied field *H* and follows a scaling law [30]:

$$-\Delta S_M^{max} \propto H^n \quad (3)$$

The field dependence of $-\Delta S_M^{max}$ and the fitting curves using Eq. (3) of both melt-spun ribbons and as-cast rods for $Gd_{55}Co_{19}Al_{24}Si_1Fe_1$ and $Gd_{20}Dy_{20}Er_{20}Co_{20}Al_{20}$ alloys are displayed in Fig. 6(a) and (b), respectively. And the obtained *n* values are listed in Table 1 as well. The *n* values are close to the values of other reported amorphous alloys and deviate from the value of 2/3 corresponding to mean field theory [2,31,32]. The larger *n* values in amorphous alloys possibly originate from the local inhomogeneity existence, e.g., chemical short-range order or impurities [33]. As listed in Table 1, the *n* values of as-cast rods are obviously larger than those of their ribbon counterparts, demonstrating that the $-\Delta S_M^{max}$ of the rods increase more rapidly with the increasing magnetic field, i.e., the rods exhibit more drastic magnetocaloric response than the ribbons with increasing magnetic field. The phenomenon that samples with the same compositions show different *n* values was analogously observed in Co-based amorphous alloys with different demagnetizing field [18,34]. The mechanical alloying or ball milled Co-based amorphous powders with larger demagnetizing field exhibit larger *n* values compared with the rapid quenching ribbons. The as-cast rods with larger diameter to length ratio exhibit larger demagnetizing field in this work, resulting in the larger *n* values. In order to compare the properties of different materials, a phenomenological universal curve for the $-\Delta S_M$ has been proposed. It is constructed by normalizing the $-\Delta S_M$ curves with respect to the ΔS_M^{max} and rescaling the temperature axis [35,36]:

$$\theta = (T - T_C)/(T_r - T_C) \quad (4)$$

where T_r is the reference temperature of each curve. The T_r corresponding to $\Delta S_M(T_r)/\Delta S_M^{max} = 0.7$ was selected in this work, and universal curves of as-cast rods and melt-spun ribbons for $Gd_{55}Co_{19}Al_{24}Si_1Fe_1$ and $Gd_{20}Dy_{20}Er_{20}Co_{20}Al_{20}$ alloys are displayed in Fig. 7(a–d). For each sample, all the normalized curves collapse onto a single curve demonstrating universal behaviors, which certifies the second order phase transition nature in these MGs [11]. The universal curve is also reported as an available method to analyze the influence of demagnetizing field, and the larger difference of reduced magnetic entropy change below T_C, the larger influence of demagnetizing field [37]. As shown in Fig. 7, the rods and ribbons shows inconspicuous difference of the reduced magnetic entropy change at the same reduced temperature, demonstrating the small demagnetizing field effect in the rods.

To further explore the difference, the morphology and the composition of the samples were detected using SEM and EDS analyses, and the results are displayed in Figs. 8 and 9. For $Gd_{55}Co_{19}Al_{24}Si_1Fe_1$ alloy, smooth ground with almost no particles can be seen on the surface of

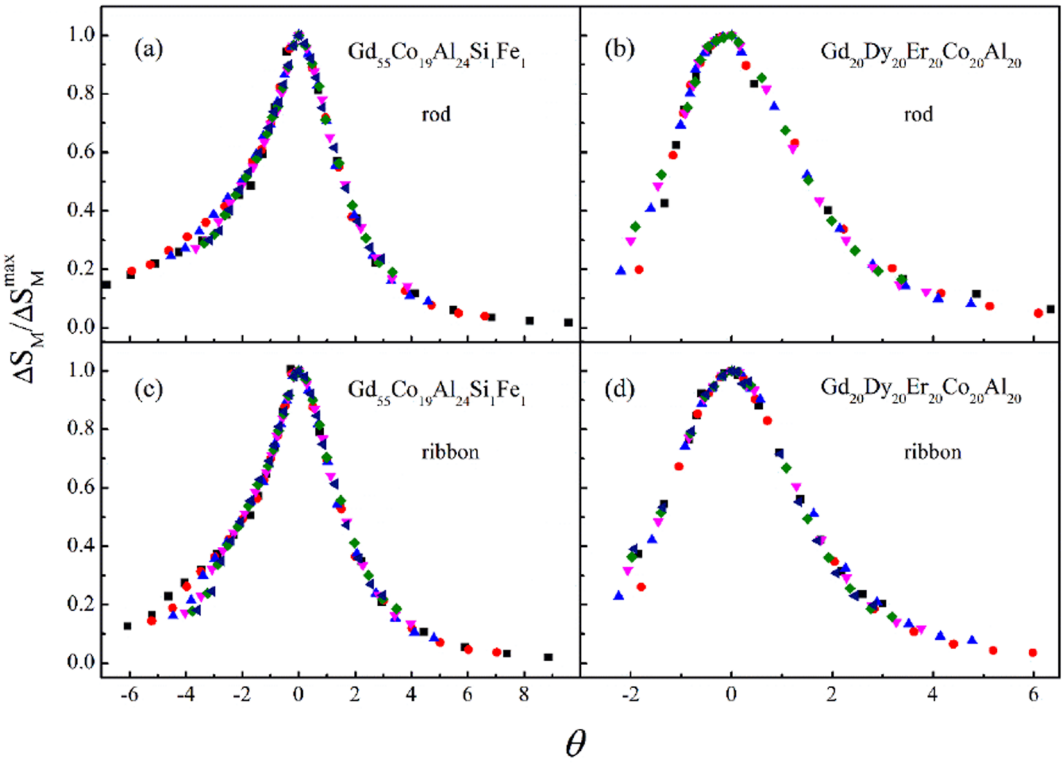

Fig. 7. Universal curves of the as-cast rods and melt-spun ribbons of $Gd_{55}Co_{20}Al_{24}Si_1Fe_1$ and $Gd_{20}Dy_{20}Er_{20}Co_{20}Al_{20}$ alloys.

the as-cast rod (Fig. 8(a)), and few pits or particles in the inner part of rod can be observed as shown in Fig. 8(b). On the contrary, particles with different sizes randomly distribute on the free surface of the melt-spun ribbon that expose to the protect atmosphere (Fig. 8(c)), besides, some particles embedded in the inner part of the polished ribbon as shown in Fig. 8(d). The compositions of the particles in the sample were detected by EDS and the microanalysis result is shown in Fig. 8(f). The detection of high intensity peaks associated to oxygen and Gd indicates that these particles would correspond to Gd oxides. As shown in Fig. 9, apparently more oxide particles can be observed in both the surfaces and the inner parts of the $Gd_{20}Dy_{20}Er_{20}Co_{20}Al_{20}$ samples than those of the $Gd_{55}Co_{19}Al_{24}Si_1Fe_1$ alloy, which can be ascribed to the higher RE content in the $Gd_{20}Dy_{20}Er_{20}Co_{20}Al_{20}$ alloy as well as the Dy and Er containing, which exhibit stronger affinity with oxygen than Gd. The detection of high intensity peaks associated to oxygen, Dy and Er indicates that the particles in this alloy would be mainly Er and Dy oxides (Fig. 9(f)). Spots are verified as RE oxides and embed in the matrix in both ribbons and rods, and the rods show apparently less oxides and impurities than the ribbons for both Gd-based MGs. Even though the ingots and samples were prepared in high vacuum and under protective argon atmosphere, oxidation is reported ineluctable for the amorphous alloys during the manufacturing [22,38]. It was reported that proper RE elements addition improves the GFA of Mg- and Fe- based alloys by scavenging oxygen impurities with the formation of innocuous RE oxides due to their stronger affinity with oxygen [24,39]. In this work, large RE oxide formation is preferred in the MGs account for their large enthalpies of formation (1819.6 kJ/mol for Gd_2O_3, 1862.7 kJ/mol for Dy_2O_3, and 1897.9 kJ/mol for Er_2O_3) and large content in the compositions [40]. Accordingly, the oxygen content in the samples were detected and the results are listed in Table 1. It is obviously that the as-cast rods contain less oxygen content than their ribbon counterparts. Compared with $Gd_{55}Co_{19}Al_{24}Si_1Fe_1$ alloy, the $Gd_{20}Dy_{20}Er_{20}Co_{20}Al_{20}$ alloy shows higher oxygen content and larger difference of oxygen content between the ribbon and rod owning to its more RE containing. These results are consistent with the SEM observation and the magnetocaloric properties.

Generally, the existence of oxides in the MGs is usually considered detrimental to the formation and properties [41]. In this work, the oxygen impurities affect the crystallization process as it induces the formation of metastable phases which act as heterogeneous nucleation sites that facilitate the crystallization, and accelerate the crystallization process, resulting in the decrease of T_x, ΔT_x as well as the crystallization enthalpy for the MGs with ribbon shape [42]. In addition, it is found that proper clusters and nanocrystallites embedded in the amorphous matrix contribute to the enhancement of magnetization and MCE for the Gd-based MGs while excess crystallizations deteriorate the magnetization and MCE [10,43]. It is well known that the cooling rate in the fabrication process of bulk samples is usually lower than that of ribbons. During the cooling process, more short-range order, medium-range order or even nanocrystallines embedded in the disordered matrix are supposed to precipitate in the rods than in the ribbons [17]. Therefore, the higher magnetization in the rods is likely related to the higher structural ordering in the samples than that of ribbons. And proper formation of short-range order and the medium-range order in the rods should improve their MCE to a certain extent. Besides, the oxide impurities in the samples should act as barriers that impede the magnetic moment rotation, and the pinning effect results in a large random magnetic anisotropy and small magnetization, thus leads to a smaller $-\Delta S_M$ and deteriorates the MCE of the MGs especially the ribbons. The formation of RE oxides embedded in the matrix, the structure heterogeneity and the demagnetizing factor account for the different magnetocaloric effect between the ribbons and rods.

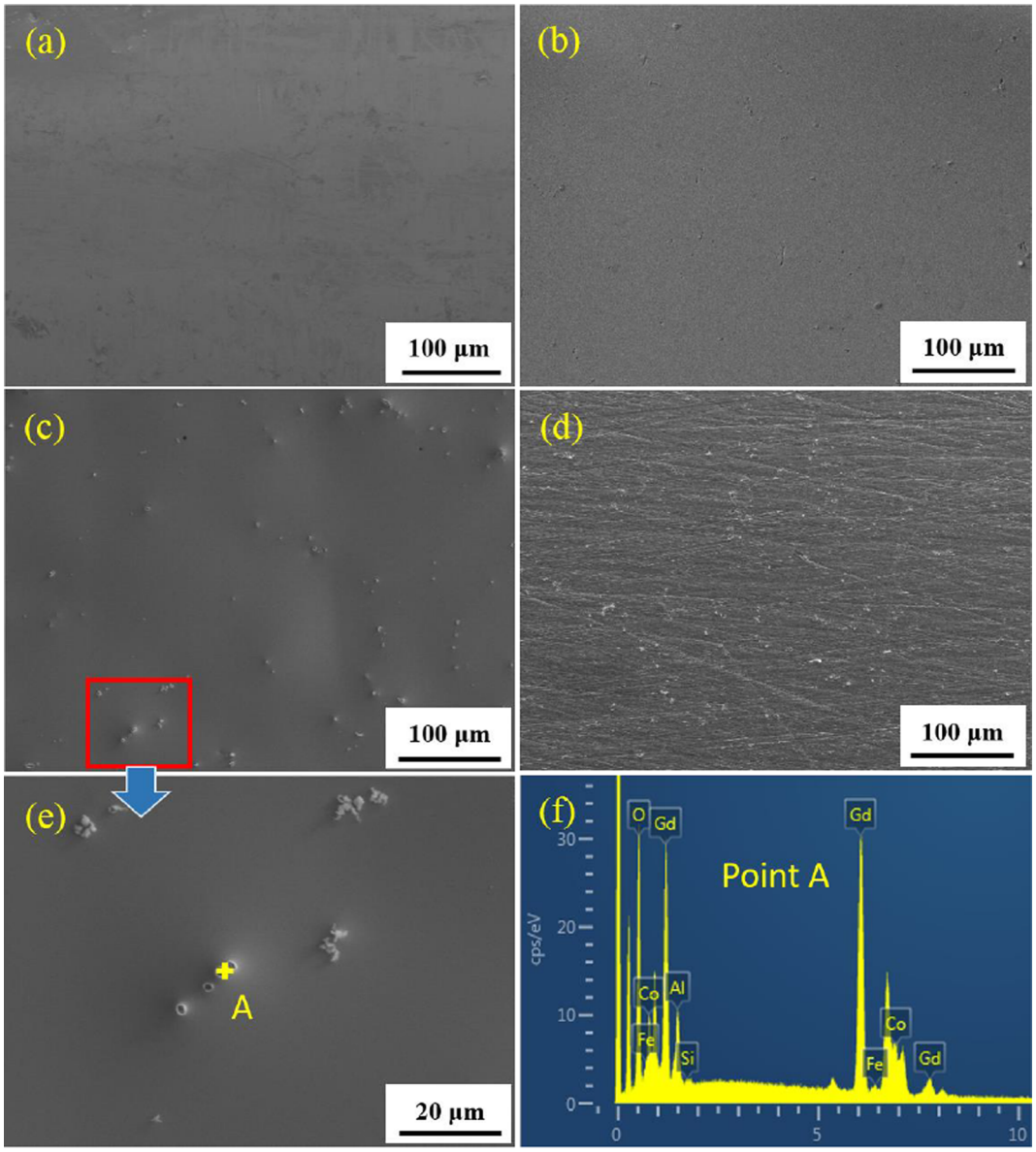

Fig. 8. SEM images of the surface (a) and inner part (b) of the rod, and the free surface (c) and the inner part (d) of the ribbon for $Gd_{55}Co_{20}Al_{24}Si_1Fe_1$ alloy. The selected region marked in (c) is magnified as shown in (e), and the EDS result of the marked particle in (e) is shown in (f).

4. Conclusion

In this work, magnetocaloric properties in the as-cast rods and melt-spun ribbons of $Gd_{55}Co_{19}Al_{24}Si_1Fe_1$ and $Gd_{20}Dy_{20}Er_{20}Co_{20}Al_{20}$ MGs are investigated. The results can be concluded as follows:

(1) Under a magnetic field change of 5 T, $-\Delta S_M^{max}$ values of 8.7 and 9.1 $Jkg^{-1}K^{-1}$ are obtained for the as-cast $Gd_{55}Co_{19}Al_{24}Si_1Fe_1$ and $Gd_{20}Dy_{20}Er_{20}Co_{20}Al_{20}$ glassy rods, respectively, which are obviously larger than those of 7.8 and 7.7 $Jkg^{-1}K^{-1}$ for their ribbon counterparts.

(2) Compared with melt-spun ribbons, the as-cast rods show larger exponent n values (i.e., the $-\Delta S_M^{max}$ increases faster as the applied magnetic field increases), which can be mainly attributed to the demagnetizing field caused by the large diameter to length ratio and local heterogeneous structures.

(3) The existence of RE oxides embedded in the samples is found to be detrimental to the formation and MCE in the RE-based magnetocaloric materials. The melt-spun ribbons with more oxides show distinctly smaller MCE comparing with the rods containing less oxides and impurities.

Declaration of Competing Interest

The authors declare that they have no known competing financial interests or personal relationships that could have appeared to influence the work reported in this paper.

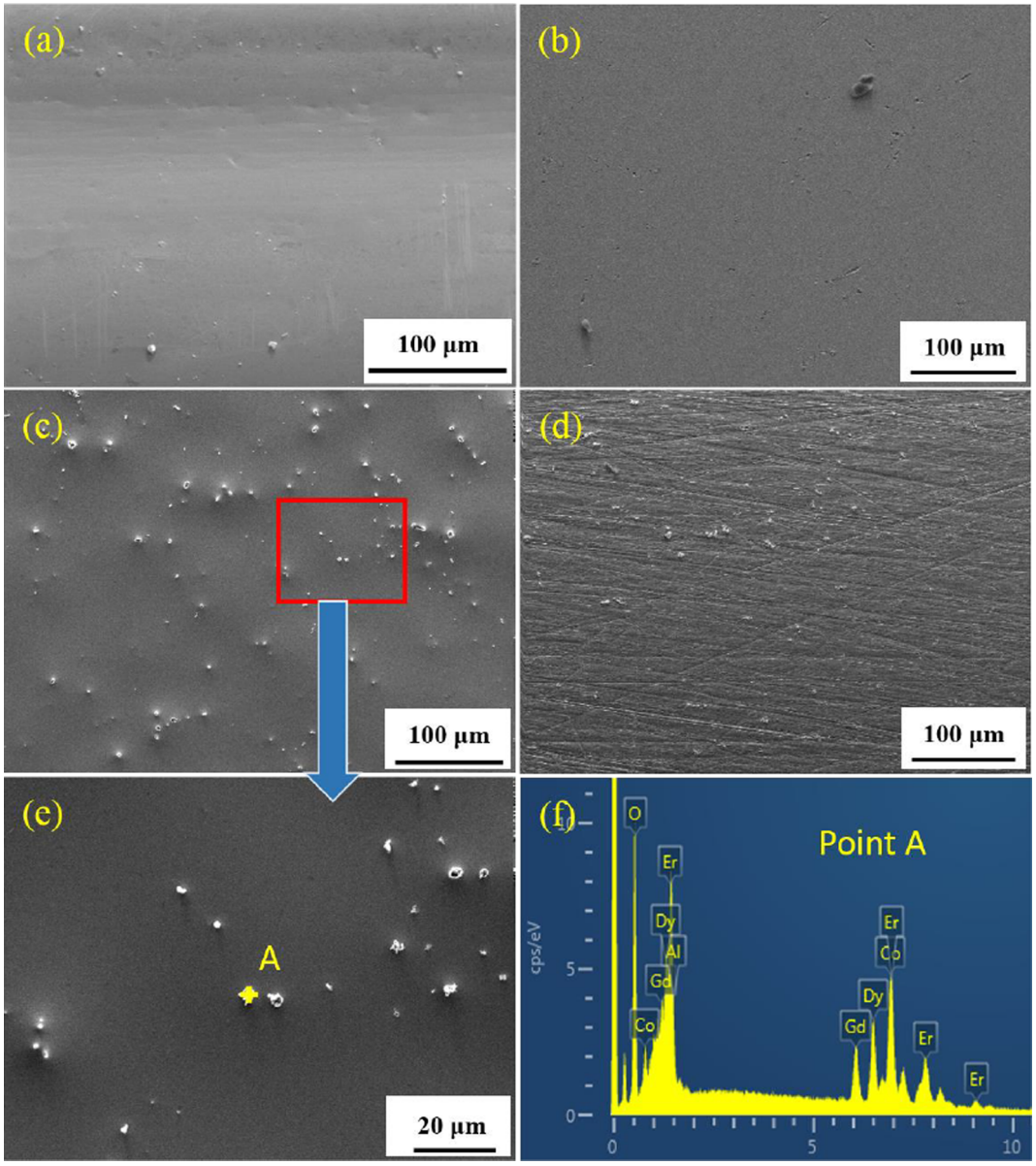

Fig. 9. SEM images of the surface (a) and inner part (b) of the rod, and the free surface (c) and the inner part (d) of the ribbon for $Gd_{20}Dy_{20}Er_{20}Co_{20}Al_{20}$ alloy. The selected region marked in (c) is magnified as shown in (e), and the EDS result of the marked particle in (e) is shown in (f).

Acknowledgements

This work was supported by the National Natural Science Foundation of China (Grant Nos. 51631003 and 51471050), the Scientific Research Foundation of Graduate School of Southeast University (Grant No. YBJJ1673), and the Fundamental Research Funds for the Central Universities (Grant Nos. 2242019K40060 and KYLX15_0121).

References

[1] K.A. Gschneidner, V.K. Pecharsky, Annu. Rev. Mater. Sci. 30 (2000) 387–429.
[2] V. Franco, J.S. Blázquez, J.J. Ipus, J.Y. Law, L.M. Moreno-Ramírez, A. Conde, Prog. Mater Sci. 93 (2018) 112–232.
[3] A.M. Tishin, Y.I. Spichkin, V.I. Zverev, P.W. Egolf, Int. J. Refrig. 68 (2016) 177–186.
[4] J. Lyubina, J. Phys. D: Appl. Phys. 50 (2017) 053002.
[5] S. Faehler, Energy Technol. 6 (2018) 1394–1396.
[6] W.M. Yang, Q.Q. Wang, H.B. Ling, H.S. Liu, L. Xue, Y.Z. He, Q. Li, B.L. Shen, J. Alloys Compd. 773 (2019) 401–412.
[7] K.A. GschneidnerJr, V.K. Pecharsky, A.O. Tsokol, Rep. Prog. Phys. 68 (2005) 1479–1539.
[8] E. Brück, O. Tegus, D.T. Cam Thanh, Nguyen T. Trung, K.H.J. Buschow, Int. J. Refrig. 31 (2008) 763–770.
[9] V.K. Pecharsky, K.A. Gschneidner, J. Magn. Magn. Mater. 200 (1999) 44–56.
[10] L.L. Shao, L. Xue, Q. Luo, Q.Q. Wang, B.L. Shen, Materiala 7 (2019) 100419.
[11] C.M. Bonilla, J. Herrero-Albillos, F. Bartolomé, L.M. García, M. Parra-Borderías, V. Franco, Phys. Rev. B 81 (2010) 224424.
[12] F. Yuan, J. Du, B.L. Shen, Appl. Phys. Lett. 101 (2012) 032405.
[13] J.T. Huo, L.S. Huo, J.W. Li, H. Men, X.M. Wang, A. Inoue, C.T. Chang, J.Q. Wang, R.W. Li, J. Appl. Phys. 117 (2015) 073902.
[14] P. Duwez, R. Willens, W. Klement Jr., J. Appl. Phys. 31 (1960) 1136–1137.
[15] H.X. Shen, D.W. Xing, J.L. Sánchez Llamazares, C.F. Sánchez-Valdés, H. Belliveau, H. Wang, F.X. Qin, Y.F. Liu, J.F. Sun, H. Srikanth, M.H. Phan, Appl. Phys. Lett. 108 (2016) 092403.
[16] H.X. Shen, H. Wang, L. Jingshun, F.Y. Cao, F.X. Qin, D.W. Xing, D.M. Chen, Y.F. Liu, J.F. Sun, J. Magn. Magn. Mater. 372 (2014) 23–26.
[17] L. Xia, Q. Guan, D. Ding, M.B. Tang, Y.D. Dong, Appl. Phys. Lett. 105 (2014) 192402.
[18] L.M. Moreno-Ramírez, J.J. Ipus, V. Franco, J.S. Blázquez, A. Conde, J. Alloys Compd. 622 (2015) 606–609.
[19] H. Fu, M.S. Guo, H.J. Yu, X.T. Zu, J. Magn. Magn. Mater. 321 (2009) 3342–3345.
[20] B. Schwarz, N. Mattern, J.D. Moore, K.P. Skokov, O. Gutfleisch, J. Eckert, J. Magn. Magn. Mater. 323 (2011) 1782–1786.
[21] V.I. Zverev, R.R. Gimaev, A.M. Tishin, Y. Mudryk, K.A. Gschneidner, V.K. Pecharsky, J. Magn. Magn. Mater. 323 (2011) 2453–2457.
[22] D.V. Louzguine-Luzgin, C.L. Chen, L.Y. Lin, Z.C. Wang, S.V. Ketov, M.J. Miyama, A.S. Trifonov, A.V. Lubenchenko, Y. Ikuhara, Acta Mater. 97 (2015) 282–290.
[23] S. González, I.A. Figueroa, I. Todd, J. Alloys Compd. 484 (2009) 612–618.
[24] C.Y. Luo, Y.H. Zhao, X.K. Xi, G. Wang, D.Q. Zhao, M.X. Pan, W.H. Wang, S.Z. Kou, J. Non-Cryst, Solids 352 (2006) 185–188.

[25] L. Xue, J. Li, W.M. Yang, C.C. Yuan, B.L. Shen, Intermetallics 93 (2018) 67–71.
[26] J. Li, L. Xue, W.M. Yang, C.C. Yuan, J.T. Huo, B.L. Shen, Intermetallics 96 (2018) 90–93.
[27] Q. Li, B.L. Shen, IEEE Trans. Magn. 47 (2011) 2490–2493.
[28] C. Wu, P. Yu, L. Xia, J. Non-Cryst Solids 422 (2015) 23–25.
[29] W.M. Yang, J.T. Huo, H.S. Liu, J.W. Li, L.J. Song, Q. Li, L. Xue, B.L. Shen, A. Inoue, J. Alloys Compd. 684 (2016) 29–33.
[30] V. Franco, A. Conde, Int. J. Refrig. 33 (2010) 465–473.
[31] V. Franco, J.S. Blázquez, A. Conde, Appl. Phys. Lett. 89 (2006) 222512.
[32] M.X. Zhang, J.W. Li, F.L. Kong, J. Liu, Intermetallics 59 (2015) 18–22.
[33] X.M. Huang, X.D. Wang, Y. He, Q.P. Cao, J.Z. Jiang, Scripta Mater. 60 (2009) 152–155.
[34] C. Romero-Muñiz, J.J. Ipus, J.S. Blázquez, V. Franco, A. Conde, Appl. Phys. Lett. 104 (2014) 252405.
[35] V. Franco, A. Conde, J.M. Romero-Enrique, J.S. Blázquez, J. Phys.: Condens. Matter 20 (2008) 285207.
[36] V. Franco, J.S. Blazquez, A. Conde, J. Appl, Phys. 103 (2008) 07B316.
[37] R. Caballero-Flores, V. Franco, A. Conde, L.F. Kiss, J. Appl. Phys. 105 (2009) 07A919.
[38] K. Weller, Z.M. Wang, L.P.H. Jeurgens, E.J. Mittemeijer, Acta Mater. 103 (2016) 311–321.
[39] X.K. Xi, R.J. Wang, D.Q. Zhao, M.X. Pan, W.H. Wang, J. Non-Cryst, Solids 344 (2004) 105–109.
[40] M. Binnewies, E. Milke, Thermochemical Data of Elements and Compounds, second ed., Wiley-VCH, Weinheim, 2002.
[41] R.D. Conner, R.E. Maire, W.L. Johnson, Mater. Sci. Eng., A 419 (2006) 148–152.
[42] A. Gebert, J. Eckert, L. Schultz, Acta Mater. 46 (1998) 5475–5482.
[43] H.F. Belliveau, Y.Y. Yu, Y. Luo, F.X. Qin, H. Wang, H.X. Shen, J.F. Sun, S.C. Yu, H. Srikanth, M.H. Phan, J Alloys Compd. 692 (2017) 658–664.